Nuclear Materials and Energy 26 (2021) 100814

Contents lists available at ScienceDirect

Nuclear Materials and Energy

journal homepage: www.elsevier.com/locate/nme

Microstructure-specific hardening of ferritic-martensitic steels pre and post 15 dpa neutron irradiation at 330 °C: A dislocation dynamics study

Michael Mahler [a,*], Giacomo Po [b], Yinan Cui [c], Nasr Ghoniem [c], Jarir Aktaa [a,*]

[a] Karlsruhe Institute of Technology (KIT), Institute for Applied Materials, Hermann-von-Helmholtz-Platz 1, 76344 Eggenstein-Leopoldshafen, Germany
[b] Department of Mechanical and Aerospace Engineering, University of Miami, Coral Gables, Miami, FL 33124, USA
[c] Department of Mechanical and Aerospace Engineering, University of California, Los Angeles, CA 90095, USA

ARTICLE INFO

Keywords:
Dislocation dynamics
Ferritic-martensitic
Eurofer
Irradiation hardening
Defect interaction

ABSTRACT

In this work, we used Dislocation Dynamics (DD) simulations to investigate the role of the hierarchical defects microstructure of ferritic-martensitic steel Eurofer97 in determining its hardening behavior. A Representative Volume Element (RVE) for DD simulation is identified based on the typical martensitic lath size. Material properties for DD simulations in b.c.c Eurofer97 are determined, including the dislocation mobility parameters. The dependence of material parameters on temperature is fitted to experimental yield strength measurements carried out at room temperature and 330 °C, respectively. Voids and precipitates observed in the microstructure, such as $M_{23}C_6$ and Tantalum-rich MX, are considered in our DD simulations as inclusions with realistic size distribution and volume density, while ⟨1 1 1⟩ -and ⟨1 0 0⟩ -type irradiation loops are included directly in the DD simulations. The lath structure, together with its typical precipitates arrangement and the different crystallographic orientation of the martensitic blocks can also be captured in the simulations. DD simulations are used to extract microstructure-specific hardening parameters, which can be used to simulate the properties of Eurofer97 at the engineering scale.

1. Introduction

Reduced activation ferritic-martensitic steels (RAFM), e.g. Eurofer97, are candidate materials for structural components of future fusion reactors because of their high strength and creep resistance, and low swelling behavior under irradiation. Compared to conventional steels, their use under high dose irradiation is preferable, because they include short-life transmutation nuclides such as W, Ta, Mn etc. resulting in strongly reduced activation. Post neutron-irradiation experiments, like WTZ 01/577 [1] and ARBOR1 [2], demonstrated that Ferritic/Martensitic (FM) steels show irradiation induced hardening with increased yield strength and loss of ductility [3]. In order to better understand the origin of irradiation-induced hardening, several microstructural investigations based on Transmission Electron Microscopy (TEM) were performed [4,5]. These studies revealed a complex hierarchical microstructure of Eurofer97, which even without irradiation is composed of austenitic-phase grain boundaries, packet/block boundaries, and martensitic laths with specific precipitates along different boundaries. In addition, irradiation induces a high density of defects such as precipitates, dislocation loops, voids/bubbles, black dots and maybe nanoclusters. Dethloff et al. [6,7,4] performed a series of post irradiation TEM analysis and studied the microstructural change after neutron irradiation in BOR-60 irradiation facility with doses of 15 and 32 displacements per atom (dpa) at irradiation temperature between 300 and 330 °C. They observed irradiation defect densities dependent on irradiation dose. The presence of irradiation defects typically leads to hardening and loss of ductility. For example, the irradiation hardening was found to be 404 MPa and 475 MPa for 15 and 32 dpa irradiation dose in the WTZ and ARBOR 1 irradiation programme, respectively [8].

A collection of defect densities based on available literature data [6,7,4] is summarized in Table 1. In the unirradiated state there are only precipitates present, while under irradiation dislocation loops and voids are formed. In addition, Dethloff et al. reported defects called black dots, which are too small to be clearly identified as loops. Under irradiation the density of precipitates keeps more or less constant. In addition, dislocation loops are visible at 15 dpa. Dethloff et al. [4] distinguished in his TEM analysis between densities of dislocation loops and dislocation loops together with black dots. For both cases, the ratio of fixed ⟨1 0 0⟩ to movable ⟨1 1 1⟩ loop densities was identified. Another defect type which was observed beyond 15 dpa are voids, although their density is low compared to that of the dislocation loops. Not visible under TEM but

* Corresponding authors.
E-mail addresses: M_Mahler@web.de (M. Mahler), jarir.aktaa@kit.edu (J. Aktaa).

https://doi.org/10.1016/j.nme.2020.100814
Received 6 January 2020; Received in revised form 14 September 2020; Accepted 16 October 2020
Available online 24 October 2020

Nomenclature

Symbols (latin)	Unit Name
a	[nm] lattice constant
A	[m] scale parameter of lognormal distribution
a_0, a_1,a_2,a_3	[-] parameters for Schmid's law
$a_{inclusion}$	[nm] lattice constant for inclusion
a_{matrix}	[nm] lattice constant for matrix
b	[nm] Burgers vector
B	[Pas] drag coefficient
B_0	[Pas] temp. indep. drag coefficient
B_1	[Pas/K] temp. dep. drag coefficient
B_e	[Pas] drag coefficient for edge dislocations
$B_{e,0}$	[Pas] temp. indep. drag coeff. for edge dislocation
$B_{e,1}$	[Pas/K] temp. dep. drag coeff. for edge dislocation
B_k	[Pas] drag coefficient for kinks
$B_{k,0}$	[Pas] temp. indep. drag coeff. for coefficient for kinks
$B_{k,1}$	[Pas/K] temp. dep. drag coeff. for coefficient for kinks
B_s	[Pas] drag coefficient for screw dislocations
$B_{s,0}$	[Pas] temp. indep. drag coeff. for coefficient for screw dislocation
$B_{s,1}$	[Pas/K] temp. dep. drag coeff. for coefficient for screw dislocations
$f(x)$	[-] lognormal distribution
G	[MPa] shear modulus
h	[nm] kink height
k_B	[J/K] Boltzmann constant
L	[nm] segment length
L_0	[nm] segment length value
m	[-] median of lognormal distribution
p	[-] fitting exponent for Kock's law
q	[-] fitting exponent for Kock's law
s	[-] standard deviation of lognormal distribution
T	[°C] or [K] temperature
T_0	[°C] or [K] transition temperature
T_m	[°C] or [K] melting temperature
v	[m/s] dislocation velocity
v_e	[m/s] edge dislocation velocity
v_s	[m/s] screw dislocation velocity
$w(\varphi)$	[-] interpolation function for edge and screw disloc. velocity

Symbols (greek)	Unit Name
ε_T	[-] transformation strain
θ	[-] ratio of shear stress and Peierls stress
ρ	[m^{-3}] defect density
ρ_L	[m^{-2}] line dislocation density
ρ_m	[kg/m^3] mass density
υ	[-] poisson ratio
σ	[-] standard deviation of lognormal distribution
σ	[MPa] stress
σ_y	[MPa] yield strength
τ	[MPa] shear stress
τ_p	[MPa] Peierls stress
ΔG_{kp}	[J] free energy of kink pair nucleation
ΔH_0	[J] enthalpy barrier for kink nucleation

Abbreviation

Name	Description
APT	Atom Probe Tomography
dpa	displacement per atom
DD	Dislocation Dynamic
MoDEL	Mechanics of Defect Evolution Library
PDD	Parametric Dislocation Dynamics
RAFM	Reduced Activation Ferritic Martensitic
RVE	Representative Volume Element
TEM	Transmission Electron Microscopy
WTZ	Nickname of an irradiation programme (15 dpa)
ARBOR1	Nickname of an irradiation programme (32 dpa)
BOR-60	Fast reactor, Riar, Russia

Table 1
Dose dependent microstructural observations after BOR-60 irradiation.

BOR-60		irradiation	
irradiation temperature ≈ 330 °C		0 dpa	15 dpa
Precipitates of type $M_{23}C_6$			
density ρ	[10^{19} m^{-3}]	5.7 [6]	5.6 [7]
Precipitates of type MX (Ta-rich)			
density ρ	[10^{19} m^{-3}]	2.4 [6]	3.9 [7]
⟨1 1 1⟩+⟨1 0 0⟩ dislocation loops			
density ρ	[10^{19} m^{-3}]	–	691 [4]
⟨1 0 0⟩ loop fraction			0.72 [4]
⟨1 1 1⟩+⟨1 0 0⟩ loops + blackdots			
density ρ	[10^{19} m^{-3}]	–	2000 [4]
⟨1 0 0⟩ loop fraction			0.45 [4]
Voids			
density ρ	[10^{19} m^{-3}]	–	36 [5]

revealed by Atom Probe Tomography (APT) are the so-called nanoclusters observed by Rogozhkin et al. [9] at higher irradiation doses. APT analysis has not been performed so far at 15 dpa, and it is unclear if nanoclusters occur at even lower irradiation dose.

In addition to defects type and density, also their size distribution plays an important role in determining the characteristics of irradiation hardening. The defects size distributions determined by TEM for unirradiated and neutron irradiated Eurofer97 of Dethloff et al. [6,7,4] can be described with the following lognormal probability distribution function:

$$f(x) = \frac{A}{\sqrt{2\pi}\sigma x} e^{\left(-\frac{(\ln(x)-m)^2}{2\sigma^2}\right)} \quad (1)$$

The parameters for each class of defects are reported in detail in section 4.2. TEM observations and post-irradiation mechanical testing have revealed the complex microstructure of RAFM steels and its influence in their hardening behavior. However, a clear quantitative relationship between microstructural parameters (e.g. defect types and size distributions) and constitutive hardening properties used in engineering design is still lacking. Unfortunately, establishing microstructure-aware constitutive laws has proved a difficult task. In fact, hardening properties are defects type and size dependent, and they require a detailed understanding of the mechanisms by which crystal dislocations interact with individual defects. This challenge is being tackled mainly by computer simulations of individual dislocations-defects interactions using the Molecular Dynamics (MD) method (see [10] for a review). Moreover, the statistical aspects of dislocations-defects interactions which emerge from their collective dynamics typically exceed the scope of atomistic computer simulations. Nonetheless, hardening and other mechanical aspects of plastic deformation in the presence of large densities of irradiation defects can be studied within the Dislocation Dynamics simulation method [11].

The objective of this work is to study hardening in Eurofer97

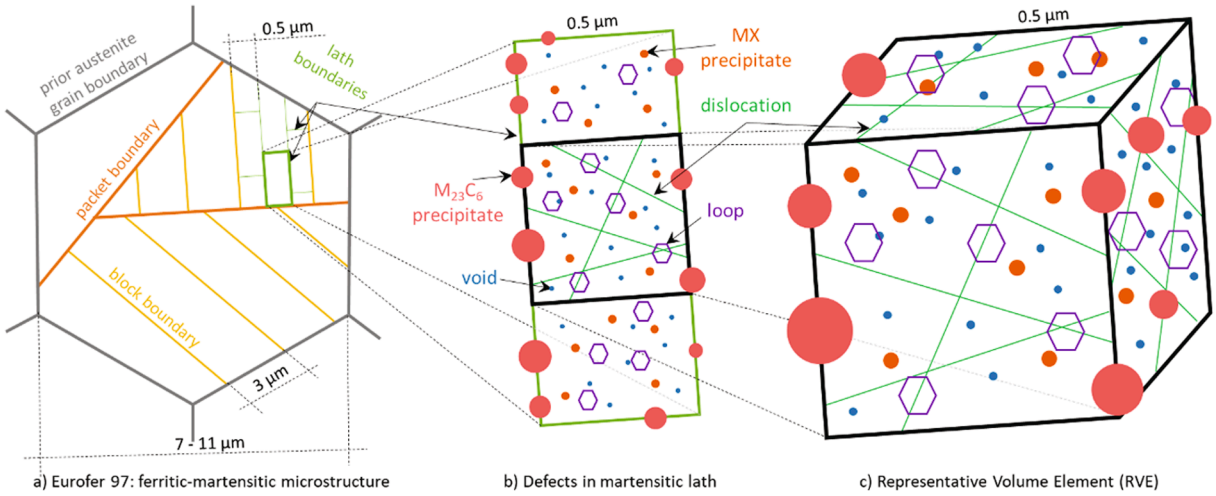

Fig. 1. Idealization of ferritic-martensitic microstructure and representative volume element.

Representative Volume Element with the dimensions of a martensitic lath.

The approach of this work will be presented in section 2. followed by the application of the approach. Therefore, the Representative Volume Element, required for the description of ferritic-martensitic microstructure, is discussed in 3. The Dislocation Dynamics simulation with all required input parameter related to Eurofer97 can be found in chapter 4 and the results are summarized in chapter 5.

2. Approach

The idea of this approach is to benefit from the experimental measurements obtained by Transmission Electron Microscopy (TEM) and learn more about irradiation induced hardening. At this, the defect densities and distributions measured for different neutron irradiation conditions can be transferred down to the level where defect interaction simulated with Dislocation Dynamics plays an important role. The principal idea goes down from the continuum time and length scale, where Engineering Problems are important, to the defect interaction level. On continuum length scale the yield strength experimentally determined increases due to neutron-irradiation. This is known as the irradiation induced hardening and it is caused by the formation and interaction of defects. These defects can be quantified by defect densities and distributions utilizing TEM. Proper Dislocation Dynamics (DD) codes like the Mechanics of Defect Evolution Library (MoDELib) developed by G. Po et al. [12] allows to study the influence of the defects. MoDEL is based on the Parametric Dislocation Dynamics (PDD) code formulated by Ghoniem et al. [13] and has its origin in the early 1990 with the work of Amodeo&Ghoniem [14].

In our case, we start on DD scale with the description of the yield strength for different temperatures. Then, additional microstructural features, which are already present without irradiation (e.g. precipitates), were added to analyze their influence. The last step is the consideration of irradiation induced defects like dislocation loops and voids. The DD simulation should be able to describe the experimentally observed increase in yield strength. Furthermore, the development of defects beyond yield can be studied.

3. The microstructure of Eurofer97 and its representation in DD simulations

The ferritic-martensitic microstructure of Eurofer97 shows a hierarchical structure. This complex microstructure [15,16,17] is illustrated in Fig. 1 a). It is defined by prior austenite grain boundaries (grey), packet boundaries (orange), block boundaries (yellow) and lath boundaries (green). The lath boundaries form the martensitic lath. The prior austenite grains (PAG) have a diameter between 6.7 and 11 µm for 14 mm thick Eurofer97 plates and 8–9.4 µm for 25 mm plates [18]. Inside the prior austenite grain boundaries there are so called packets, which are separated by packet boundaries (PB). A packet is characterized by blocks with the same set of parallel planes, but with different crystallographic orientations [19]. The block itself contains martensitic laths with same crystallographic orientation [19]. The typical dimension of a block measured by EBSD is about 3.1 µm [16]. In such a hierarchical structure, no Representative Volume Element (RVE) can be rigorously defined. Here we simply consider the smallest unit of the hierarchical structure of Eurofer97, the martensitic lath with its boundaries. Hence, the martensitic lath is used as the Representative Volume Element (RVE) in our DD simulations. This choice is mainly justified by space–time limitation of the DD method, although it is also supported by the physical consideration that the lath boundaries precipitates partially restrict the dislocation activity across them. However, it is recognized that this choice might limit the prediction of the true bulk behavior of the material, since we ignore other characteristic length scales associated with block, packet, and grain boundaries.

Table 2
Yield strength dependent on temperature [8].

	0 dpa			15 dpa	32 dpa
Temperature T in [°C]	23	330	550	330	330
Yield strength σ_y in [MPa]	544	465	345	869	940

The size of the martensitic laths determined by TEM [20] is in the range of 0.5 ± 0.2 µm. Fig. 1 b) shows a martensitic lath and all features relevant for irradiation hardening. The lath boundaries (lime green) are sub-grain boundaries, which are formed in this case out of $M_{23}C_6$ precipitates (red) [6,7]. They are large and composed of Cr, Fe, W and C. In addition, there are small Ta rich MX precipitates (orange) present, which are located inside the lath [6]. Other precipitates are of minor importance, because their concentration is very low. In addition to the precipitates, there are free line dislocations (dark green) within the lath with a line density ρ_L of around 0.9E14 m^{-2} [21]. All mentioned defects so far are present in the initial microstructure without influence of irradiation.

Due to its microstructure, the ferritic-martensitic steel has good deformation and creep properties. The yield strength dependence on temperature and irradiation dose is listed in Table 2.

The yield strength increases dramatically. At 330 °C the yield strength for 15 dpa increases around 404 MPa compared to the

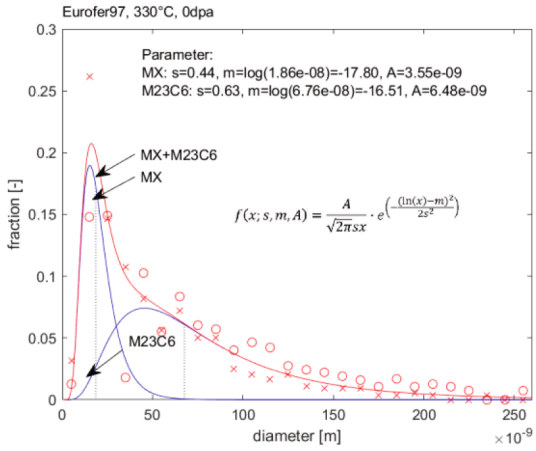

a) MX and $M_{23}C_6$ precipitates, unirradiated [6]

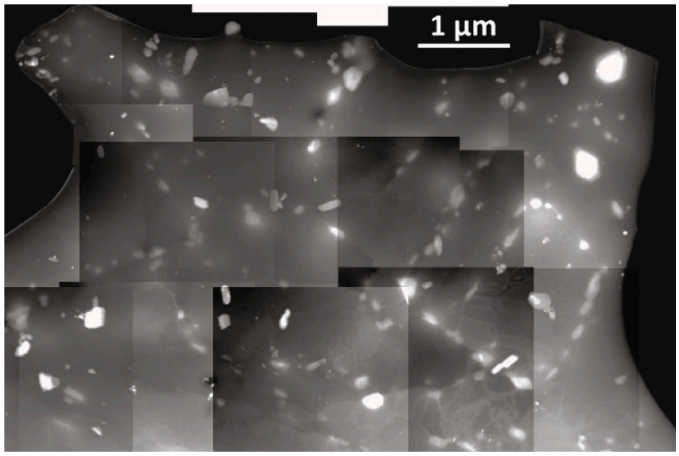

b) TEM micrograph showing precipitates of unirradiated Eurofer97 [6]

Fig. 2. Precipitates and TEM micrograph without irradiation.

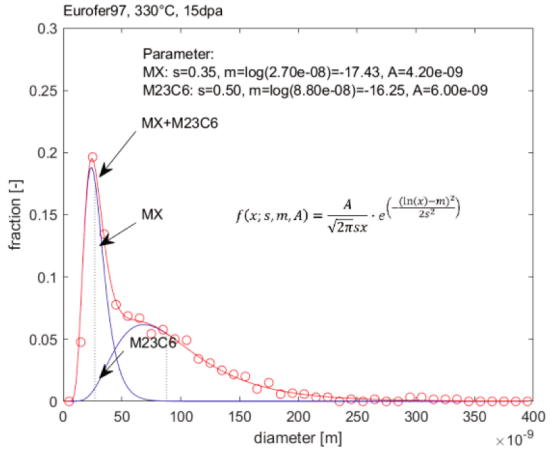

a) MX and $M_{23}C_6$ precipitates, irradiated 15 dpa [6]

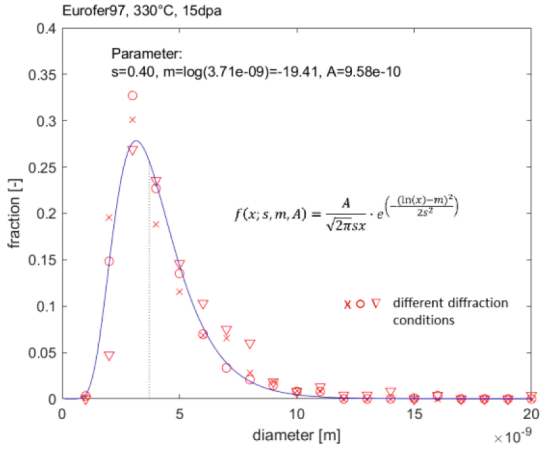

b) Loops, irradiated 15 dpa [4]

Fig. 3. Precipitates and dislocation loops after 15 dpa irradiation.

unirradiated state. Even between 15 dpa and 32 dpa there is still an increase of around 71 MPa, but it seems to saturate. The yield strength of the unirradiated material will be used later for a comparison with the simulation result. If the yield strength can be simulated, it is assumed that the mobility law can be used for additional simulations related to irradiation hardening. This work focuses on the irradiation dose of 15 dpa and higher irradiation doses are planned for the future.

Next, we shall consider the defects content of both unirradiated and 15 dpa irradiated Eurofer97, with the objective of extracting probability size distribution parameters of different defect families for later use in DD simulations. In general, the defects content measured in the TEM studies of Dethloff et al. ([6,7,4]) can be fitted to following lognormal probability size distribution function:

$$f(x) = \frac{A}{\sqrt{2\pi}\sigma x} e^{\left(-\frac{(\ln(x)-m)^2}{2\sigma^2}\right)} \tag{2}$$

Here σ and m refer to the standard deviation and the mean values of the lognormal distribution function, respectively.

In the case of unirradiated Eurofer97, the defects population is mainly composed of two families of precipitates of type $M_{23}C_6$ and MX, respectively. The size distribution of these precipitates was measured on two specimens by Dethloff et al. [6]. The defect distributions for $M_{23}C_6$ and MX were fitted with two lognormal distributions. The average curve for each precipitate type is shown in Fig. 2a with blue color for MX and $M_{23}C_6$ precipitates, respectively. The red curve is the sum of both average lognormal distributions (see parameters in Fig. 2a) and describes the measurement in good agreement. The mean diameter of MX type precipitates is 18.6 nm and for $M_{23}C_6$ precipitates, it is 67.6 nm. Fig. 2b shows a TEM micrograph, where the martensitic laths formed by $M_{23}C_6$ precipitates are visible. Other defect types have not been observed in the unirradiated state.

The $M_{23}C_6$ and MX precipitates content observed by Dethloff et al. [6] following neutron irradiation (15 dpa at 330 °C) is shown in Fig. 3a with red circles. These defects populations were averaged and fitted with two lognormal distributions. The red solid line shows the sum of both lognormal distributions. The mean diameter of $M_{23}C_6$ precipitates is 88.6 nm and for MX type 27.6 nm.

In addition to altering the precipitates content, irradiation also leads to the generation of new defects families, namely ⟨100⟩ and ⟨111⟩ dislocation loops [4]. The mean diameter of the loops is 3.7 nm. The distribution is shown in Fig. 3b. Dethloff et al. [4] performed a critical assessment of the visibility of loops and the TEM resolution limit. In this context, the mean diameter of loops and so called black dots is equal to 3.3 nm, and the ⟨100⟩ loop fraction is equals 0.45. The defect

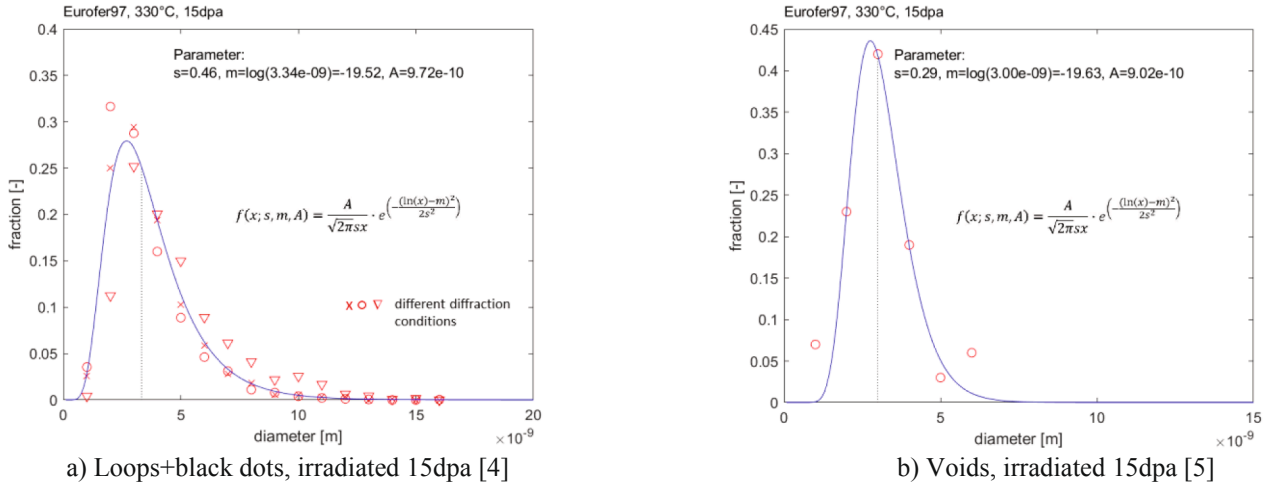

Fig. 4. Dislocation loops + black dots and voids after 15dpa irradiation.

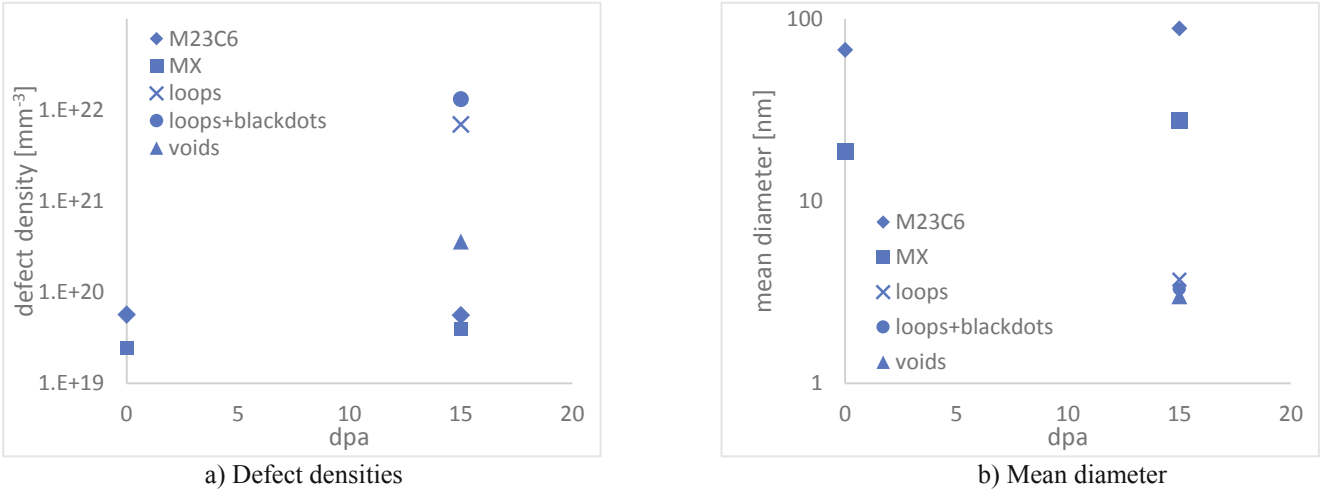

Fig. 5. Summary of defect densities and mean diameters.

distribution including loops and black dots is shown in Fig. 4a, together with its log-normal fitting and parameters. It is assumed that the size of the mean diameter of black dots is about 1 nm.

Voids are another defect type which occurs during irradiation of Eurofer97. Voids have been identified with mean size of 3 nm [5]. The corresponding lognormal distribution is shown in Fig. 4b.

Fig. 5a shows the densities of all defect types in the unirradiated state and after 15 dpa to summarize the presented defect densities. It is obvious that for $M_{23}C_6$ and MX type precipitates the defect density is independent from irradiation dose. Beyond 15 dpa the loops and black dots show the highest defect density. Fig. 5 b) compares the evolution of mean diameter with and without irradiation according to [6]. In general, there is a slight increase in mean diameter visible for the precipitates.

4. Dislocation Dynamics simulation

In this section, the basic equations of the mobility law developed and implemented by G. Po et al in DD code MoDEL are presented. The equation for the velocity of kinks was slightly modified regarding temperature dependence. Furthermore, within this chapter the parameters used for the ferritic-martensitic steel Eurofer97 will be shown.

4.1. Mobility law

For a good description of dislocation mobility, a proper mobility law must be used. The Dislocation Dynamics code MoDEL is based on a phenomenological mobility law developed by Po et al. [12]. This mobility law was developed for b.c.c. metals. Tungsten has been chosen by Po et al. as an example material for demonstration of its applicability. The formulation of the mobility law is limited to the glide component of dislocation motion and climb (controlled by diffusion of point defects) is not considered. The general form of the mobility law, see equation (3), is given as

$$v(\sigma,T,\varphi)=v_s(\sigma,T)[1-w(\varphi)]+v_e(\sigma,T)[w(\varphi)] \quad (3)$$

It is a function of temperature T and stress σ. Furthermore, it interpolates between screw dislocation velocities v_s and edge dislocation velocities v_e with a specific interpolation function $w(\varphi)$. More details can be found in Po et al. [12]. With this interpolation function, a smooth transition between kink-dominated and phonon dominated regime is guaranteed [12]. The general form of dislocation velocity (edge or screw) is implemented in the DD code with equation (4) as:

$$v(\sigma,T)=\begin{cases}\dfrac{\tau b}{B(\sigma,T)}\exp\left(-\dfrac{\Delta G_{kp}(\sigma,T)}{2k_BT}\right) & \text{if } \Delta G_{kp}(\sigma,T)>0\\ \dfrac{\tau b}{B(\sigma,T)} & \text{if } \Delta G_{kp}(\sigma,T)\le 0\end{cases} \tag{4}$$

The dislocation velocity is dependent on the resolved shear stress τ and the product τb is the glide component of the Peach-Koehler force [12]. The velocity can be influenced by the drag coefficient$B(\sigma,T)$, which depends on stress and temperature.

The distinction of cases by $\Delta G_{kp}(\sigma,T)$ allows differentiating between active and non-active kink-pair mechanisms. If the free energy of kink pair nucleation $\Delta G_{kp}(\sigma,T)$ is greater or equal to zero, the kink diffusion model influences the behaviour of dislocation velocity. This kink diffusion model depends on the Boltzmann k_B, the temperature and the free enthalpy, see equation (5)

$$\Delta G_{kp}(\sigma,T)=\Delta H_0\left\{[1-\theta(\sigma)^p]^q-\frac{T}{T_0}\right\} \tag{5}$$

In this equation the fitting constant T_0 can be interpreted as an athermal transition temperature above which the energy barrier for kink-pair nucleation is guaranteed [12]. The remaining part in this equation is based on the phenomenological law introduced by Kocks [22]. The variable ΔH_0 is the enthalpy barrier for kink nucleation and the exponents p and q are used as fitting parameters. With the ratio $\theta=\tau/\tau_p$, defined by the resolved shear stress τ and Peierls stress τ_p, the free enthalpy can be described.

Po et al. [12] introduced the drag coefficient dependent on kink pair activation. If the free enthalpy is bigger than zero, the drag coefficient depends on the thermally activated kink process. In the other case, the drag coefficient follows a linear relationship dependent on temperature, see equation (6)

$$B(\sigma,T)=\begin{cases}\dfrac{a\left[2aexp\left(\dfrac{\Delta G_{kp}(\sigma,T)}{2k_BT}\right)+L\right]}{2hL}B_k & \text{if } \Delta G_{kp}(\sigma,T)>0\\ B_0+B_1T & \text{if } \Delta G_{kp}(\sigma,T)\le 0\end{cases} \tag{6}$$

In this equation, we use for the lattice constant a, the kink height h and the segment length L the relations in equations (7)-(9) derived from the geometry of the bcc lattice:

$$a=\frac{2}{\sqrt{3}}b \tag{7}$$

$$h=\frac{2\sqrt{2}}{3}b \tag{8}$$

$$L=L_0b \tag{9}$$

Although phonon scattering theory suggests a temperature-dependent drag coefficient, the drag coefficient for kinks B_k used in Po et al. [12] is independent from temperature. In this work we did not explore the details of the drag behavior of kinks. We simply assume a linear relationship between temperature and drag coefficient, in the form

$$B_k=B_{k,0}+B_{k,1}T \tag{10}$$

where we simply consider $B_{k,0}$ and $B_{k,1}$ as fitting constants. The combination of the equations above allows now the final definition of edge and screw dislocation velocities.

edge dislocation velocity

The edge dislocation velocity in equation (11) is dominated by phonon drag regime. The kink dominated regime is equal to zero and it is independent from the free energy of kink pair nucleation:

$$v_e(\sigma,T)=\frac{\tau b}{B_e(\sigma,T)}\quad\text{with}\quad B_e(\sigma,T)=B_{e,0}+B_{e,1}T \tag{11}$$

Table 3
Material properties for Eurofer97.

Property	Symbol	Unit	Value
Melting temperature	T_m	[°C]	1538
Lattice constant [23]	a	[nm]	0.2484
Burgers vector ⟨1 1 1⟩ [23]	b	[nm]	0.2868
Shear modulus [24]	G	[MPa]	$G=G_0+G_1T$
Poisson ratio [24]	ν	[-]	0.3
Mass density [24]	ρ_m	[kg/m^3]	7670

Table 4
Dislocation Dynamics related material parameters for Eurofer97.

Property	Symbol	Unit	dislocation screw	edge	
Enthalpy barrier for kink nucleation	ΔH_0	[eV]	0.65	≈ 0	[25]
Mobility exponent	p	[-]	0.5	–	[25]
Mobility exponent	q	[-]	1.25	–	[25]
Athermal transition temperature	T_0	[°C]	$0.138T_m$	–	[26]
Peierls stress	τ_p	[MPa]	360	–	[27,28]
Non-schmid coefficient	a_0	[-]	1.0	–	[29]
Non-schmid coefficient	a_1	[-]	0.4577	–	[29]
Non-schmid coefficient	a_2	[-]	0.1454	–	[29]
Non-schmid coefficient	a_3	[-]	0.5645	–	[29]
Drag coefficient kink	$B_{k,0}$	[Pas]	6.60E-5	–	[30]
Drag coefficient kink	$B_{k,1}$	[Pas/K]	−3.80E-7	–	[30]
Drag coefficient screw/edge	$B_{s,0}$; $B_{e,0}$	[Pas]	7.83E-5	9.65E-6	[30,25]
Drag coefficient screw/edge	$B_{s,1}$; $B_{e,1}$	[Pas/K]	2.71E-8	6.42E-7	[30,25]
Segment length	L_0	[-]	30.5		[31]

screw dislocation velocity

For screw dislocations both regimes – phonon drag and kink dominated – are relevant. Equation (12) show the final formulae of drag coefficient for screw dislocations:

$$v_s(\sigma,T)=\frac{\tau b}{B_s(\sigma,T)}\ \text{with}\ B_s(\sigma,T)$$
$$=\begin{cases}\dfrac{\sqrt{3}\left[\dfrac{4}{\sqrt{3}}exp\left(\dfrac{\Delta G_{kp}(\sigma,T)}{2k_BT}\right)+L_0\right]}{2\sqrt{2}L_0}(B_{k,0}+B_{k,1}T) & \text{if } \Delta G_{kp}(\sigma,T)>0\\ B_{s,0}+B_{s,1}T & \text{if}\Delta G_{kp}(\sigma,T)\le 0\end{cases} \tag{12}$$

4.2. Parameters for Eurofer97

Our material of interest is the ferritic-martensitic steel Eurofer97 with its b.c.c. crystal structure. Some general material properties like melting temperature, lattice constant, Burgers vector, shear modulus, Poisson ratio and mass density are listed in Table 3.

Based on a literature study the remaining parameters used in the equations of section 4.1 are summarized in Table 4 and will be explained in more detail on the following pages.

The athermal transition temperature T_0 used in equation (5) can be defined based on the work of H. Conrad [26]. He studied the temperature dependence of the activation energy for pure iron and pure chromium. Pure iron reaches its plateau for an activation energy of 0.56 eV at around 230 Kelvin and pure chromium for 1.0 eV at higher temperature. If we now consider that the chromium content in Eurofer97 is about 9% we can calculate an activation energy of 0.65 eV for the level of the plateau and this is reached at a temperature of around 350 Kelvin

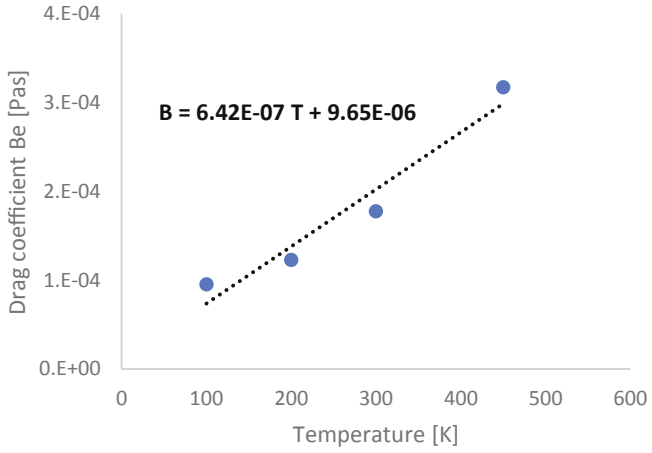

Fig. 6. Phonon drag coefficients edge dislocations.

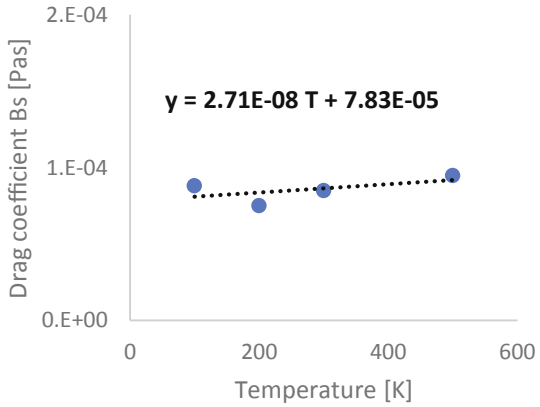

Fig. 7. Phonon drag coefficient for screw dislocations.

and will be used as athermal transition temperature T_0.

The Peierl's stress τ_p, see equation (5), for b.c.c. iron mentioned in Gururiaj [27] is in very good agreement with single crystal yield stress experimental data at zero Kelvin [28]. The reported value is 360 MPa and used within this work.

It is well-known that the screw dislocations in bcc metals is largely affected by non-Schmid effects [12]. The mobility law employed in this work is sensitive to the non-Schmid components of stress. We implement a well established model [32], which predicts the onset of slip of a screw dislocations when the shear stresses on the planes of the [1 1 1] zone satisfy the condition

$$a_0\tau_p = \tau_{(\bar{1}01)} + a_1\tau_{(0\bar{1}1)} + a_2\tau'_{(\bar{1}01)} + a_3\tau'_{(0\bar{1}1)} \tag{13}$$

The non-Schmid parameters in equation (13) for b.c.c iron have been determined by Chen [24] ($a_1 = 0.4577$, $a_2 = 0.1454$, $a_3 = 0.5645$). The parameter a_0 was not specified and it was set equal to 1.0 to be consistent with the implementation in DD code MoDEL. Comparable non-Schmid parameters were reported by Köster et al. [33], which proofs their applicability.

At sufficiently high stress and temperature, the dislocation mobility is dominated by the phonon drag rather than kink nucleation and migration. Therefore, the mobility law includes drag coefficients for edge and screw dislocations and also for kinks. The phonon drag coefficients of edge dislocations used for Eurofer97 are based on the work of Queyreau et al. [25]. They determined the edge dislocation mobility for b.c.c. iron by molecular dynamics. The drag coefficient for edge dislocations increases linearly with temperature and its value approximately triples between 100 and 450 K [25], see Fig. 6.

The equation of the linear fitting is shown in equation (14):

$$B_e = B_{e,0} + B_{e,1}T = 9.65 \cdot 10^{-6} + 6.42 \cdot 10^{-7}T \tag{14}$$

Gilbert et al. [30] identified the dependence of stress and temperature of screw dislocation mobility in b.c.c. iron. In this context, they determined phonon drag coefficients for screw dislocations and kinks. The equation for screw dislocation velocity mentioned in his work uses the normal stress instead of the shear stress. For this reason the Taylor factor ($M = 3.06$) must be considered to transfer shear stresses to normal stresses, see equation (15):

$$\sigma = M\tau = 3.06\tau \tag{15}$$

In case of screw dislocations, the dependence of phonon drag coefficient on temperature considering the Taylor factor is shown in Fig. 7 according to [30].

The equation of the linear fitting is shown in equation (16):

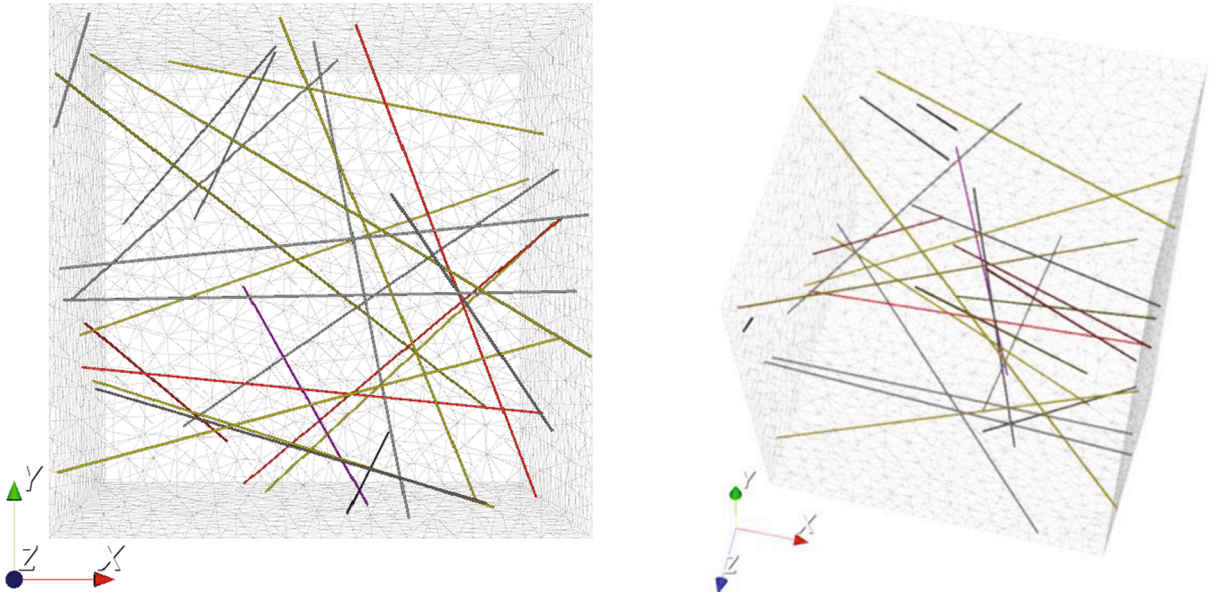

Fig. 8. Initial microstructure for line dislocations.

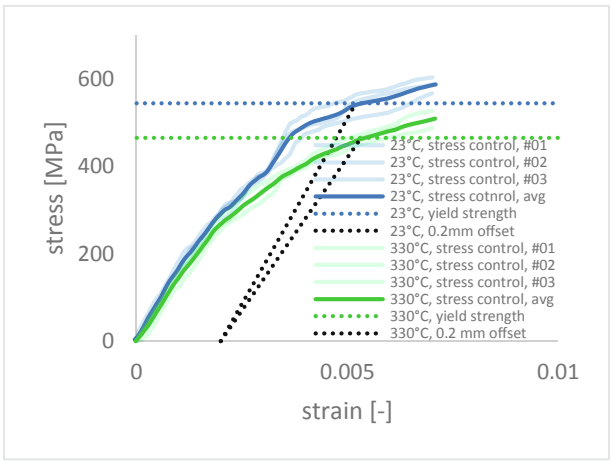

a) Temperature dependence of yield strength

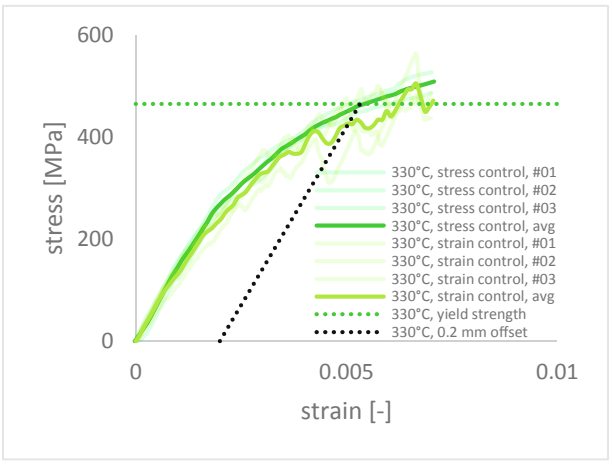

b) Dependence of stress- & strain-rate control

Fig. 9. DD simulation results.

$$B_s = B_{s,0} + B_{s,1}T = 7.83 \cdot 10^{-5} + 2.71 \cdot 10^{-8}T \tag{16}$$

For the formation of kinks in the thermally activated regime the drag coefficient was determined by fitting based on a satisfied description of the experimental yield strength in Table 2. The equation of the linear fitting is shown in equation (17):

$$B_k = B_{k,0} + B_{k,1}T = 6.6 \cdot 10^{-5} - 3.8 \cdot 10^{-7}T \tag{17}$$

The last unknown parameter for the mobility law is the segment length L_0, which is used in equation (12). Brunner&Diehl [31] reported a value of 30.5 for the segment length L_0 which is used within this work.

5. Results and discussion

This paragraph shows the simulation results obtained with the Representative Volume Element presented in Fig. 1 c). All simulations are based on the defect densities and defect distributions presented within this work. For the dislocation mobility, the parameters summarized in Table 3 and Table 4 were used.

Section 5.1 starts with the simulation of yield strength dependence on temperature. The influence of additional features like inclusions ($M_{23}C_6$ or MX precipitates) are discussed in section 5.2. The last part (section 5.3) deals with the influence of irradiation induced hardening on the yield strength.

5.1. Simulation of the temperature dependence of yield strength

In this section, the temperature dependence of yield strength is presented. The DD simulations were performed at room temperature and 330 °C. The obtained yield point from the simulation at these temperatures is compared with the experimental yield strength. The line dislocation density used for the Representative Volume Element (RVE) was 0.9E14 m^{-2}. The initial microstructure was generated randomly with a specific generator for line dislocations, see Fig. 8.

In a first step, precipitates were not included, because it is assumed, that their influence on yield strength will be minor. The RVE needs a grain orientation, which can be defined with a so called grain orientation matrix in MoDEL, see equation (18).

$$M = \begin{bmatrix} 1 & 0 & 0 \\ 0 & 1 & 0 \\ 0 & 0 & 1 \end{bmatrix} \tag{18}$$

The simulations were performed under stress- and strain-rate control. The strain-rate is equal to 1000 s^{-1} and the used stress-rate has been chosen corresponding to this strain-rate. For room temperature as well as for 330 °C, the drag coefficient for kinks was changed until the simulation was able to reproduce the experimental yield strength. This procedure has been chosen due to lacking literature data.

Fig. 9 a) shows the result of the DD simulation under stress-rate control. For room temperature, there are three curves in light blue and the average curve in deep blue. For 330 °C the same is shown in green color. The horizontal dotted blue and green lines show the experimental yield strength. It is obvious that due to fitting the average curves for both temperatures fits the experimental yield strength very well.

The influence between stress- and strain-rate control at 330 °C is presented in Fig. 9 b). The light lime green curves show the result of three simulations under strain-rate control. All these curves show remarkable drops in stress, which is caused by the constant strain rate. The lime green curve shows the average curve under strain-rate control. A comparison of the deep and lime green average curves shows, that the difference between stress-rate and strain-rate control is not significant.

5.2. Simulation of the influence of precipitates

The microstructure of Eurofer97 shows $M_{23}C_6$ precipitates, which are located predominantly at the lath boundaries, see Fig. 1. In consequence, their influence on yield strength should be minor. Nevertheless, there are Ta-rich MX precipitates inside the lath and they may affect the yield strength of the material.

In the MoDEL implementation used here, dislocations interact among themselves and with the irradiation loops through their elastic stress field. The stress field is then used in the mobility law to determine the time evolution of the dislocation microstructure configuration. Precipitates interact with dislocations by providing an additional source of stress in the material, and by acting as obstacles to the motion of dislocations. In order to investigate the effects of precipitation, we have implemented the stress field of precipitates according to Eshelby inclusions theory [34]. For simplicity precipitates are implemented as spherical inclusions in the DD code MoDEL. The interaction between precipitates and dislocations is governed by the stress field of the inclusion. In turn, this depends on the so called transformation strain of the inclusion. In our work, the transformation strain is assumed to be isotropic transformation associated with the lattice constant mismatch between inclusion and matrix. This can be calculated according to equation (19):

$$\varepsilon_T = \frac{a_{inclusion} - a_{matrix}}{a_{matrix}} \tag{19}$$

For a first guess the precipitates are treated as impenetrable, which cannot be sheared (inclusion problem). This means, that the

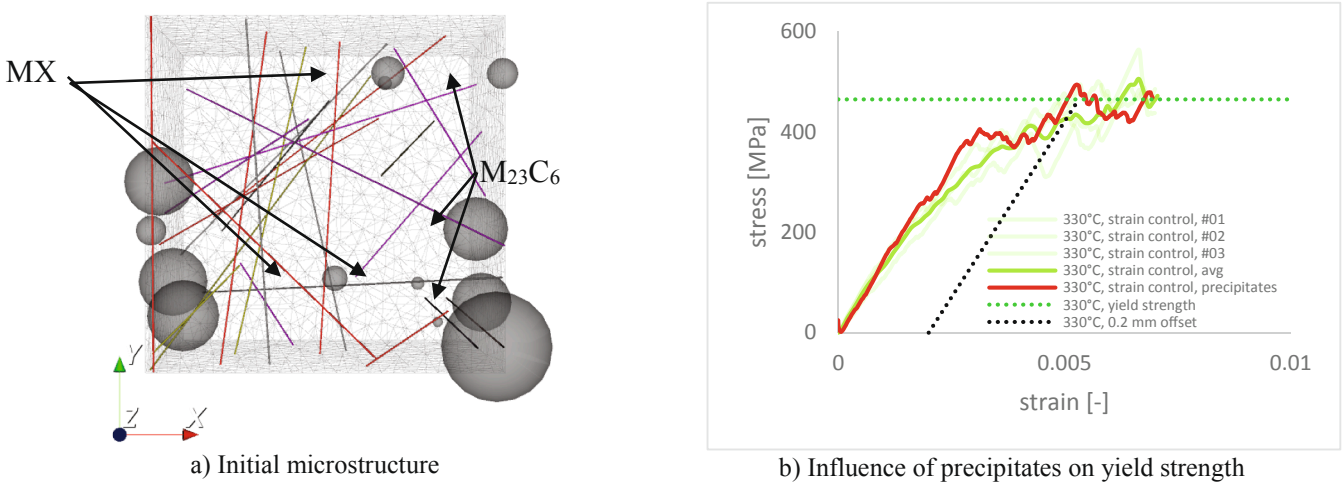

Fig. 10. Microstructure and DD simulation results.

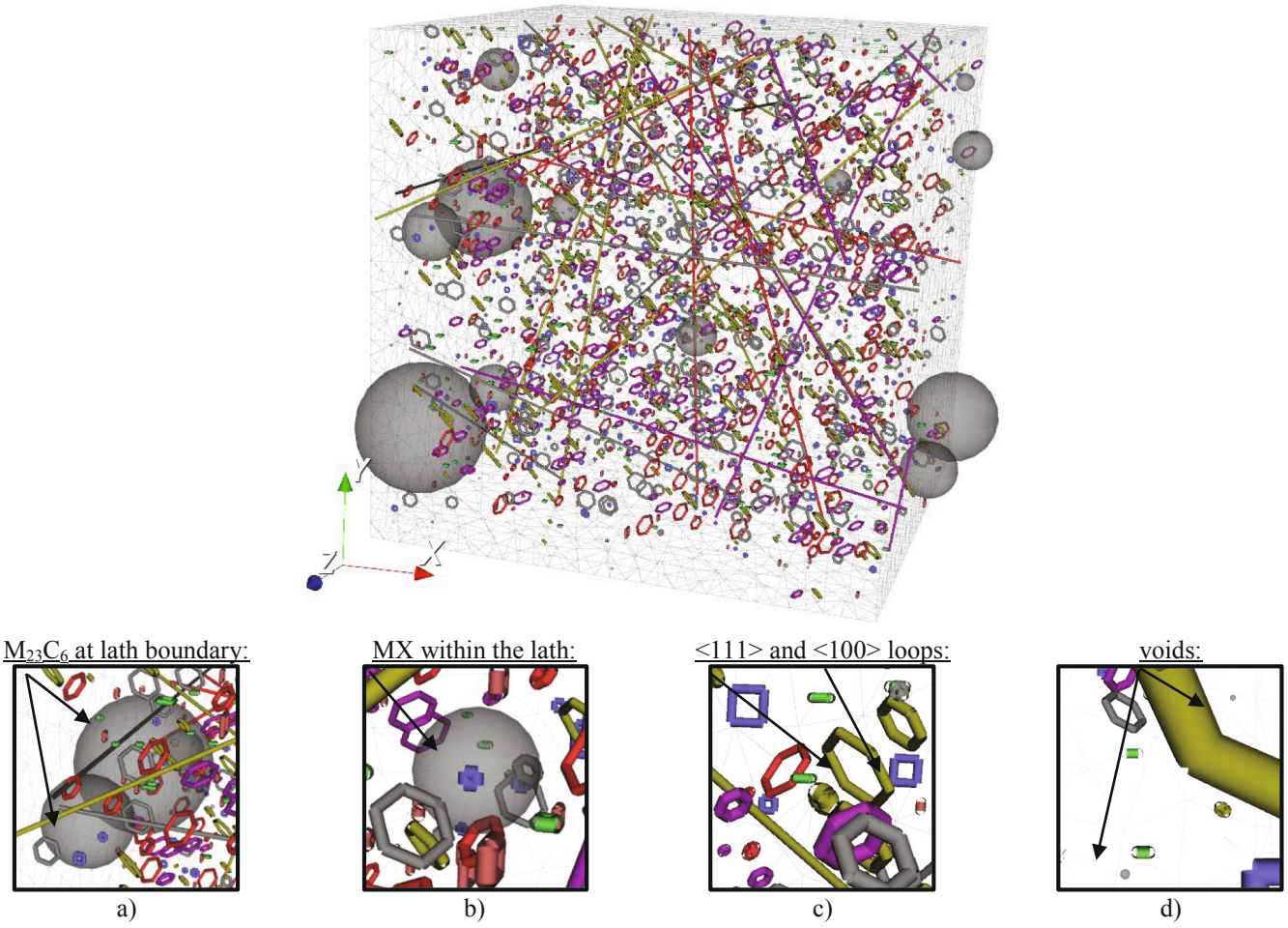

Fig. 11. Initial microstructure for line dislocations, precipitates, dislocation loops and voids.

impenetrable inclusion should have a strong influence on the general behavior. The simulation has been performed at 330 °C under strain-rate control with initial line dislocation density of 0.9E14 m^{-2}. Furthermore, the densities and lognormal distributions of $M_{23}C_6$ and MX-type precipitates (see Fig. 2) were added before generating the microstructure. The initial microstructure used in the RVE is shown in Fig. 10 a). The spheres lying at the outer surfaces of the RVE represents the $M_{23}C_6$ precipitates and the ones within the volume are the MX-type precipitates. It is important to mention that these inclusions do not have specific material properties. These spherical volumes are impenetrable and cannot be sheared by any dislocation.

The simulation result obtained with precipitates under strain-rate control at 330 °C is compared with the result without precipitates in Fig. 10 b). The red curve clearly shows, that the influence of precipitates

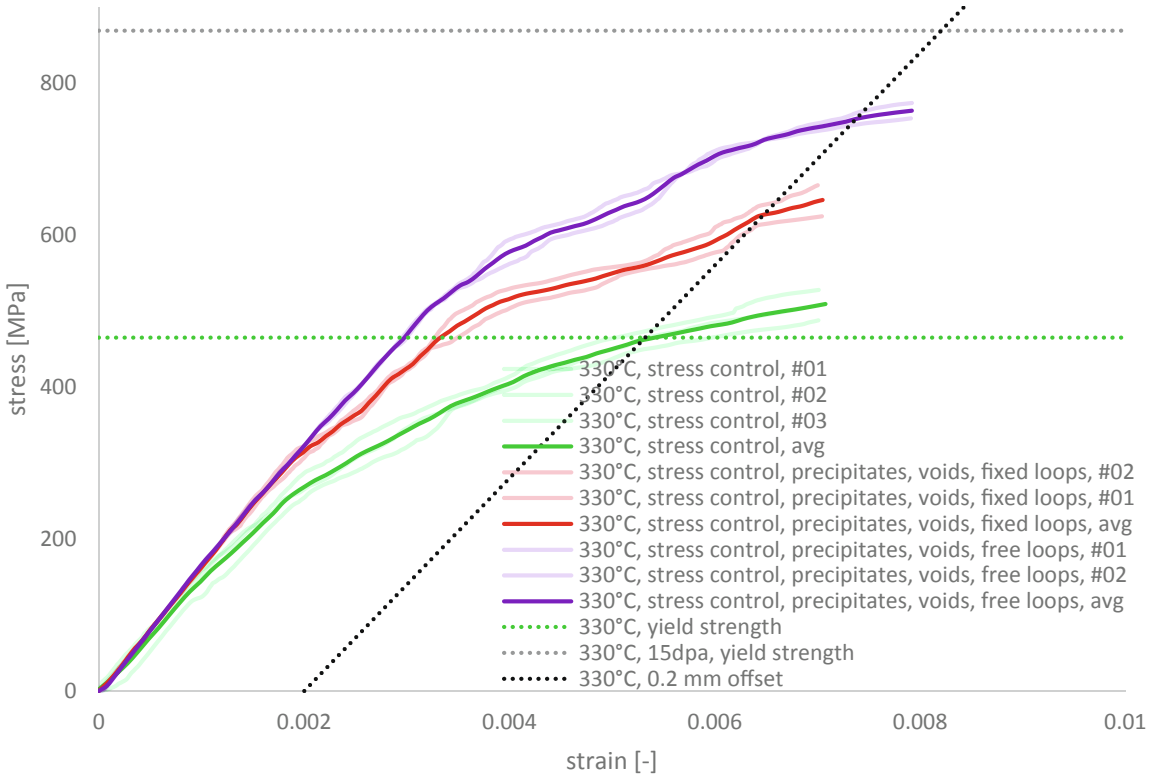

Fig. 12. DD simulation results considering irradiation induced hardening.

treated as impenetrable inclusions is minor compared to the green curves obtained with line dislocations, only. However, the precipitates will be maintained for further simulations, because it is not clear how their influence after irradiation will be.

5.3. Simulation of irradiation induced hardening

Dethloff et al. [6 7 4] observed dislocation loops and voids inside the lath after 15 dpa neutron irradiation. After re-evaluation of TEM measurement, Dethloff [4] reported defect densities and distributions for dislocation loops and black dots, see Fig. 4. The analyzed loops have the types $\langle 1\,0\,0 \rangle$ as well as $\langle 1\,1\,1 \rangle$. The DD simulation is able to consider the ratio of $\langle 1\,0\,0 \rangle$ and $\langle 1\,1\,1 \rangle$ loops, which was experimentally measured by TEM [4]. The initial microstructure for DD simulation considers now the distribution and densities of precipitates, loops + blackdots and voids. All defect features generated with the microstructure generator are visualized in Fig. 11.

In addition to the grey spheres, representing the precipitates in Fig. 11 a) & b), there are $\langle 1\,1\,1 \rangle$ and $\langle 1\,0\,0 \rangle$ loops added (loops with 4 and 6 corners), see Fig. 11 c). The corners forming the loops have the same features as line dislocations and all $\langle 1\,0\,0 \rangle$ loops are fixed at their initial position. The $\langle 1\,1\,1 \rangle$ loops have in general two options depending on the simulation settings:

- Fixed position
- Free movement

The neutron irradiation generates voids within the microstructure, which have been considered as impenetrable small inclusions; see Fig. 11 d). Hence, the dislocation voids interaction neglects the free surface effects and image forces [35,36], respectively. The distribution and density of voids was set according to TEM measurements by Weiß et al. [5], see Fig. 4.

In a first simulation, all dislocation loops were fixed at their initial position and cannot move. The simulation result at 330 °C under stress-rate control after 15 dpa neutron irradiation (considered with corresponding defect densities and distributions) is shown in Fig. 12 with the curve in red color. Compared to the green curve before irradiation, there is an increase in yield strength visible. This increase is called irradiation induced hardening based on the formation of defects like dislocation loops and voids. The experimental yield strength after neutron irradiation of 15 dpa was equal to 869 MPa with an increase from unirradiated to irradiated case of 404 MPa. The simulation shows a less pronounced increase in yield strength (223 MPa). In summary, the simulation predicts a yield strength after irradiation, which is equal to 627 MPa.

The reason for the discrepancy between experiment and simulation of irradiation induced hardening can be versatile:

- Dislocation loop or void density obtained by TEM is not correct
- Dislocation loop or void distribution obtained by TEM is not correct
- Ratio for $\langle 1\,1\,1 \rangle$ and $\langle 1\,0\,0 \rangle$ loops obtained by TEM is not correct
- $\langle 1\,1\,1 \rangle$ loops should not be fixed at all

To figure out the discrepancy between simulation and experiment, another simulation has been performed, where the $\langle 1\,1\,1 \rangle$ dislocation loops have the possibility to move within the RVE. After 15 dpa the presence of the $\langle 1\,1\,1 \rangle$ dislocation loops dominate with 55% compared to the $\langle 1\,0\,0 \rangle$ loops. This means that around half of all loops will have the opportunity to move in this simulation. The simulation result is shown in Fig. 12 with purple color. The influence of irradiation hardening on yield strength is more pronounced compared to the simulation before, where all dislocation loops are fixed on their initial position. The simulated yield strength now increases to 752 MPa and the increase in yield strength is equal to 287 MPa.

These simulations have shown, that the movement of $\langle 1\,1\,1 \rangle$ dislocation loops increases the irradiation induced hardening significantly. Nevertheless, there is still a gap between experiment and simulation. If we now assume, that the TEM resolution limit does not allow detecting defects smaller than one nanometer, it is obvious that there are more defects present than observed by TEM. Additional small defects e.g.

small loops in DD simulations would act as obstacles and affect the movement of line dislocations and ⟨1 1 1⟩ loops. For this reason, other techniques than TEM, like Atom Probe Tomography (APT), should be considered to be able to quantify small particles in the future.

6. Conclusion

This paper shows the effect of irradiation hardening based on the interaction of defects by Dislocation Dynamics simulations. Initially the ferritic-martensitic microstructure of Eurofer97 was discussed. The main finding was, that it is sufficient to simulate a Representative Volume Element with the dimensions of a martensitic lath. Based on that, the microstructural features forming the lath were figured out. In the following, a literature survey on irradiation induced hardening based on TEM observations was presented. The most relevant information for the Dislocation Dynamics simulations were the type of defects with their densities and defect distributions. All defect distributions from literature were fitted with lognormal distributions. The corresponding parameters were summarized to use them in the simulations.

The DD simulation requires a proper mobility law. Within this work, the mobility law for b.c.c. materials developed by Po et al. [12] has been used with a small modification regarding the temperature dependence of the drag coefficient for kinks B_k.

The simulations focused on three main parts:

- The proper description of the material yield strength,
- the influence of precipitates on yield strength and
- the influence of irradiation induced defects on the yield strength.

It was shown, that the precipitates have a minor influence on yield strength and could be neglected. The dislocation loops and voids, formed under neutron irradiation, influence the yield strength significantly. It is important to notice that the movement of dislocation loops within the volume affects the yield strength in addition. There is still a gap between the yield strength after irradiation observed in the experiment and the simulation. In the future, other experimental techniques like Atom Probe Tomography would help to identify small defects (smaller than one nanometer). If their density and distribution were known, it would be easy to add them to a DD simulation to be able to simulate the experimental yield strength after irradiation.

CRediT authorship contribution statement

Michael Mahler: Conceptualization, Methodology, Writing - original draft. **Giacomo Po:** Supervision, Writing - review & editing. **Yinan Cui:** Supervision, Writing - review & editing. **Nasr Ghoniem:** Supervision, Writing - review & editing. **Jarir Aktaa:** Supervision, Writing - review & editing.

Declaration of Competing Interest

The authors declare that they have no known competing financial interests or personal relationships that could have appeared to influence the work reported in this paper.

Acknowledgement

This work has been carried out within the framework of the EUROfusion Consortium and has received funding from the Euratom research and training programme 2014-2018 and 2019-2020 under grant agreement No 633053. The views and opinions expressed herein do not necessarily reflect those of the European Commission.

References

[1] C. Petersen, J. Aktaa, E. Diegele, E. Gaganidze, R. Lässer, E. Lucon, E. Marterna-Morris, A. Möslang, A. Povstyanko, V. Prokhorov, J. Rensman, B. von der Schaaf and H.-C. Schneider, "Mechanical Properties of Reduced Activated Ferritic/Martensitic Steels after European Reactor Irradiations," in 21st IAEA Fusion Energy Conference, China, 2006.
[2] C. Petersen, V. Shamardin, A. Fedoseev, G. Shimansky, V. Efimov, J. Rensman, The ARBOR irradiation project, J. Nucl. Mater. 307–311 (2002) 1655–1659.
[3] E. Gaganidze, J. Aktaa, Assessment of neutron irradiation effects on RAFM steels, Fusion Eng. Des. 88 (3) (2013) 118–128.
[4] C. Dethloff, E. Gaganidze, J. Aktaa, Review and critical assessment of dislocation loop analyses on EUROFER 97, Nuclear Materials and Energy 15 (2018) 23–26.
[5] O. Weiß, E. Gaganidze, J. Aktaa, Quantitative charaterization of microstructural defects in up to 32 dpa neutron irradiated EUROFER97, J. Nucl. Mater. 426 (2012) 52–58.
[6] C. Dethloff, E. Gaganidze, J. Aktaa, Quantitative TEM analysis of precipitation and grain boundary segregation in neutron irradiated EUROFER 97, J. Nucl. Mater. 454 (1-3) (2014) 323–331.
[7] C. Dethloff, E. Gaganidze, J. Aktaa, Microstructural defects in EUROFER 97 after different neutron irradiation conditions, Nuclear Materials and Energy 9 (2016) 471–475.
[8] C. Petersen, "Post irradiation examination of RAF/M steels after fast reactor irradiation up to 33 dpa and <340°C (ARBOR1), FZKA 7517," Karlsruhe, 2010.
[9] S. Rogozhkin, A. Nikitin, N. Orlov, A. Bogachev, O. Korchuganova, A. Aleev, A. Zaluzhnyi, T. Kulevoy, R. Lindau, A. Möslang, P. Vladimirov, Evolution of microstructure in advanced ferritic-martensitic steels under irradiation: the origin of low temperature radiation embrittlement, Energy and Sustainability 2 (21–22) (2017) 1143–1155.
[10] D. Bacon, Y. Osetsky, D. Rodney, Dislocation - obstacle interactions at the atomic level, Dislocations in solids 15 (2009) 1–90.
[11] J. Marian, S. Fitzgerald, G. Po, Discrete dislocation dynamics simulations of irradiation hardening in nuclear materials, in: W. Andreoni, S. Yip (Eds.), Handbook of Materials Modeling, Springer, Cham, 2018, pp. 1–29.
[12] G. Po, Y. Cui, D. Rivera, D. Cereceda, T.D. Swinburne, J. Marian, N. Ghoniem, A pehnomenological dislocation mobility law for bcc metals, Acta Mater. 119 (2016) 123–135.
[13] N.M. Ghoniem, S.-H. Tong, L.Z. Sun, Parametric dislocation dynamics: A thermodynamics-based approach to investigations of mesoscopic plastic deformation, Phys. Rev. B 61 (2) (2000) 913–927.
[14] R.J. Amodeo, N.M. Ghoniem, Dislocation dynamics I. A proposed methodology for deformation micromechanics, Phyiscal Review B 41 (1990) 6958–6967.
[15] F. Barcelo, Y. de Carlan, J.-L. Béchade, B. Fournier, Orientation relationship in Eurofer martensitic steels, Phase Transitions 82 (11) (2009) 808–820.
[16] M.F. Giordana, P.-F. Giroux, I. Alvarez-Armas, M. Sauzay, A. Armas, T. Kruml, Microstructure evolution during cyclic tests on EUROFER 97 at room temperature. TEM observation and modelling, Mater. Sci. Eng., A 550 (2012) 103–111.
[17] D. Litvinov, A. Chauhan and J. Aktaa, "Microstructural evolution of 9Cr-ODS steel during high temperature deformation," in European Microscopy Congress 2016: Proceedings, Lyon, 2016.
[18] P. Fernandez, A.M. Lancha, J. Lapena, M. Hernandez-Mayoral, Metallurgical charaterization of the reduced activiation ferritic/martensitic steel Eurofer97 on as-received condition, Fusion Eng. Des. 58–59 (2001) 787–792.
[19] K.D. Zilnyk, V.B. Oliveira, H.R.Z. Sandim, A. Möslang, D. Raabe, Martensitic transformation in Eurofer-97 and ODS-Eurofer steels: A comparative study, J. Nucl. Mater. 462 (2015) 360–367.
[20] P. Fernandez, A. M. Lancha, J. Lapena, M. Serrano and M. Hernandez-Mayoral, "Reduced Activation Ferritic/Martensitic Steel Eurofer97 as Possible Structural Material for Fusion Devices, Metallurgical Characterization on As-Received Condition and after Simulated Service Conditions," Ciemat, 2004.
[21] L. Straßberger, Untersuchung und Modellierung des viskoplastischen Verformungsverhaltens oxidpartikelverstärkter Stähle, KIT, Karlsruhe, 2017.
[22] U. Kocks, A. Argon, M. Ashby, Thermodynamics and kinetics of slip, Progress Materials Science 19 (1975) 1–281.
[23] K. Mergia, N. Boukos, Structural, thermal, electrical and magnetic properties of Eurofer 97 steel, J. Nucl. Mater. 373 (1-3) (2008) 1–8.
[24] CEA, "Appendix A - Material design limit data: A3.19AS Eurofer - TBM steel," CEA, 2010.
[25] S. Queyreau, J. Marian, M. R. Gilbert and Wirth B D, "Edge dislocation mobilities in bcc FE obtained by molecular dynamics," Physical Review B, vol. 84, no. 064106, 2011.
[26] H. Conrad, W. Hayes, Thermally-Activated Deformation of the Body Centered Cubic Metals at Low Temperatures, Commander Space Systems Division, United States Air Force, Inglewood, California, 1963.
[27] K. Gururaj, C. Robertson, M. Fivel, Post-irradiation plastic deformation in bcc Fe grains investigated by means of 3D dislocation dynamics simulation, J. Nucl. Mater. 459 (2015) 194–204.
[28] S. Takaki, D. Akama, N. Nakada, T. Tsuchiyama, Effect of grain boundary segregation of interstitial elements on Hall-Petch coefficient in steels, Mater. Trans. 55 (1) (2014) 28–34.
[29] Z. Chen, Modelling the plastic deformation of iron, KIT Scientific Publishing, Karlsruhe, 2013.
[30] M.R. Gilbert, S. Queyrequ, J. Marian, Stress and temperature dependence of screw dislocation mobility in alpha-Fe by molecular dynamics, Physical Review B 84 (2011), 174103.

[31] D. Brunner, J. Diehl, Temperature and Strain-Rate Dependence of the Tensile Flow Stress of High-Purity alpha iron below 250 K (II), Physica Status Solidi (A) 125 (1991) 203.
[32] R. Gröger, A. Bailey, V. Vitek, Multiscale modeling of plastic deformation of molybdenum and tungsten: I. Atomistic studies of the core structure and glide of 1/2⟨111⟩ screw dislocations at 0K, Acta Mater. 56 (19) (2008) 5401–5411.
[33] A. Koester, A. Ma, A. Hartmeier, Atomistically informed crystal plasticity model for body-centered cubic iron, Acta Mater. 60 (2012) 3894–3901.
[34] T. Mura, Micromechanics of Defects in Solids, Second revised edition, Dordrecht, Boston, Martinus Nijhoff Publishers, Lancester, 1987.
[35] S.M. Hafez Haghighat, M.C. Fivel, J. Fikar, R. Schaeublin, Dislocation–void interaction in Fe: A comparison between molecular dynamics and dislocation dynamics, J. Nucl. Mater. 386-388 (2009) 102–105.
[36] Joshua C. Crone, Lynn B. Munday, Jaroslaw Knap, Capturing the effects of free surfaces on void strengthening with dislocation dynamics, Acta Mater. 101 (2015) 40–47.